applied sciences

MDPI

Article

Enhanced Methylene Blue Removal over Expanded Vermiculite-Supported Fe_3O_4 Heterogeneous Fenton-like System: Parameter Optimization and Degradation Mechanisms

Ye Zhang [1,†], Xinyu Yang [2,†], Xiaogang He [1], Wenfei Wu [1], Dan Sun [2,*] and Haiyan Tao [1,*]

[1] Xinjiang Key Laboratory of New Functional Materials Chemistry, College of Chemical and Environmental Sciences, Kashi University, Kashi 844000, China; zy992999214@163.com (Y.Z.); 17809211562@163.com (X.H.)
[2] College of Chemistry and Chemical Engineering, Tarim University, Alar 843300, China
* Correspondence: sundan2991@163.com (D.S.); taohaiyan0728@163.com (H.T.)
† These authors contributed equally to this work.

Abstract

Expanded vermiculite (EVMT) is a low-cost layered silicate, yet bare Fe_3O_4 suffers from severe aggregation and poor stability in Fenton-like systems. Herein, an EVMT-supported Fe_3O_4 composite (Fe_3O_4@EVMT) was prepared by co-precipitation to remove methylene blue (MB). Scanning electron microscopy (SEM), X-ray diffraction (XRD), and X-ray photoelectron spectroscopy (XPS) confirmed that Fe_3O_4 nanoparticles were well-dispersed on layered EVMT, which effectively alleviated particle aggregation and offered abundant surface-active sites. Single-factor experiments were performed to investigate the influences of initial pH, catalyst dosage and H_2O_2 concentration on MB elimination. Box–Behnken response surface methodology was further adopted for multi-parameter optimization. Under optimized conditions (pH 3.8, catalyst 1.0 g/L, H_2O_2 4.5 mmol/L), the MB removal efficiency reached 98.26%. The degradation process fitted well with the pseudo-second-order kinetic model, and the calculated activation energy was 40.2 kJ/mol, suggesting that chemical oxidation dominated the reaction. Radical-quenching tests combined with electron paramagnetic resonance spectra verified that hydroxyl radicals (·OH) functioned as the predominant reactive species, while superoxide radicals ($\cdot O_2^-$) played a secondary role. Low iron-leaching concentration was detected throughout the reaction. After five successive recycling tests, the catalyst still maintained above 80% MB removal efficiency, demonstrating acceptable reusability. This mineral-based catalyst is promising for dye wastewater treatment, though further tests on real wastewater are required for practical application.

Keywords: vermiculite; response surface methodology; Fe_3O_4; methylene blue; Fenton-like reaction

Academic Editor: Jaecheul Yu

Received: 30 October 2026
Revised: 22 November 2026
Accepted: 25 November 2026
Published: 26 November 2026

Copyright: © 2026 by the authors. Licensee MDPI, Basel, Switzerland. This article is an open access article distributed under the terms and conditions of the Creative Commons Attribution (CC BY) license.

1. Introduction

Methylene blue (MB) is a typical cationic thiazine dye widely used in textile dyeing, biological staining, and other industrial applications [1,2]. Wastewater generated from its production and utilization exhibits high chromaticity, strong biological toxicity, poor biodegradability and long residual duration. Upon accumulation through the food chain, MB may threaten human health and poses potential carcinogenic and teratogenic hazards [3]. Traditional water-treatment techniques, including coagulation-sedimentation, biodegradation and adsorption [4], are incapable of fully decomposing the stable

conjugated chromophore structure of MB. Such approaches are restricted by low degradation efficiency, considerable secondary pollution and narrow applicability, and thus can not satisfy current environmental requirements for advanced industrial-wastewater treatment.

Advanced oxidation processes (AOPs) characterized by powerful oxidation capacity can effectively break stable chemical bonds of organic contaminants and achieve complete mineralization, rendering them core technologies for treating refractory organic dye-containing wastewater [5]. As one representative AOP, Fenton-like oxidation degrades pollutants through free-radical species (·OH and $\cdot O_2^-$) produced by hydrogen-peroxide activation. This strategy possesses multiple merits such as rapid reaction kinetics, convenient operation and low secondary pollution, and overcomes the limitations of conventional homogeneous Fenton systems, including a narrow effective pH range, substantial iron-sludge generation and difficult catalyst recovery [6,7]. Fe_3O_4 particles are classic magnetic iron-based catalyst, that enable reversible redox conversion between Fe^{2+} and Fe^{3+} and exhibit excellent magnetic separability. They can efficiently activate H_2O_2 to produce hydroxyl (·OH) and superoxide ($\cdot O_2^-$) radicals and be readily recovered from water, which qualify them as a promising Fenton-like catalyst. Nevertheless, pristine Fe_3O_4 nanoparticles suffer from severe agglomeration, insufficient exposed active sites [8,9], and this issue markedly impairs their catalytic performance and hinders practical engineering deployment. Support-immobilization modification has emerged as an effective strategy to enhance the catalytic performance of iron-based materials. Vermiculite (VMT) is a natural layered silicate mica mineral belonging to the phyllosilicate group. Expanded vermiculite (EVMT) is mainly produced by thermal exfoliation through rapid heating in industrial practice, and chemical expansion is an alternative laboratory route to obtain porous EVMT. Its unique layered architecture facilitates the dispersion of Fe_3O_4 nanoparticles on its external surfaces, suppresses particle agglomeration and increases the density of surface-active sites [10,11]. Compared with other frequently reported supports for heterogeneous Fenton-like catalysts such as conventional natural clays, zeolites, and biochar, the EVMT displays distinctive comprehensive merits. Untreated natural clays generally possess compact interlayer structures, which hinder the uniform dispersion of Fe_3O_4 nanoparticles and provide limited exposed active sites [12]. Although zeolites are featured with well-defined microporous frameworks, their narrow pore channels are susceptible to blockage after Fe_3O_4 loading, restraining mass-transfer of large-sized dye molecules [13]. Biochar is regarded as an economical candidate support; nevertheless, its physicochemical properties are highly susceptible to feedstock varieties and pyrolysis parameters, resulting in unsatisfactory batch-to-batch reproducibility [14]. By contrast, EVMT is naturally abundant and cost-effective, which generates a layered-porous architecture that facilitates firm immobilization and homogeneous dispersion of Fe_3O_4 nanoparticles. Moreover, the polar hydroxyl-rich surface of EVMT can adsorb and concentrate cationic MB molecules around catalytic active sites, shortening the diffusion path between organic pollutants and reactive oxygen species and achieving favorable adsorption-catalysis synergy [15]. Despite these advantages, most existing EVMT-based Fenton catalysts only rely on single-factor screening, while the interactive effects of key operating parameters remain poorly quantified. In addition, the underlying radical degradation pathway and catalyst stability under variable reaction conditions still require systematic clarification. Response surface methodology (RSM) can construct multivariate quadratic regression models to systematically evaluate interactive effects among experimental variables and precisely determine optimal operational parameters. Compared with single-factor experiments, RSM minimizes experimental bias and optimizes testing schemes, and has been widely utilized for parameter

optimization in water-treatment research [16,17].

In the study, an expanded-vermiculite-supported Fe_3O_4 composite catalyst (Fe_3O_4@EVMT) was synthesized to establish a heterogeneous Fenton-like system. Response surface methodology (Box–Behnken design) was adopted to systematically investigate the effects of catalyst dosage, H_2O_2 concentration and initial pH on MB degradation efficiency, analyse the interaction effects between these variables and optimize degradation conditions. The catalytic stability and reusability of the prepared Fe_3O_4@EVMT were also evaluated. This work is expected to provide a theoretical basis for the application of magnetic clay-based composite catalysts in printing-dyeing wastewater remediation.

2. Materials and Methods

2.1. Materials

Raw vermiculite was supplied by Xinjiang Yuli Xinlong Vermiculite Co., Ltd. (Yuli, China). Methylene blue, tert-butanol and 5,5-dimethyl-1-pyrroline-N-oxide (DMPO) were purchased from Macklin Chemical Reagent Co., Ltd. (Shanghai, China). Ferrous sulfate heptahydrate ($FeSO_4{\cdot}7H_2O$) and ferric chloride hexahydrate ($FeCl_3{\cdot}6H_2O$) were obtained from Sinopharm Chemical Reagent Co., Ltd. (Shanghai, China). Hydrogen peroxide (H_2O_2, 30 wt%), benzoquinone, hydrochloric acid (HCl) and sodium hydroxide (NaOH) were acquired from Aladdin Biochemical Technology Co., Ltd.(Shanghai, China).

2.2. Synthesis of the Fe_3O_4@EVMT

The raw vermiculite was soaked in 30 wt% H_2O_2 aqueous solution for 48 h for chemical expansion to obtain EVMT. The resultant EVMT was pulverized using a high-speed electric grinder and sieved through a 200-mesh sieve. The collected EVMT powder was stored under dry conditions for subsequent use.

0.3 g of $FeSO_4{\cdot}7H_2O$, 0.584 g of $FeCl_3{\cdot}6H_2O$ (Fe^{2+}/Fe^{3+} molar ratio = 1:2), and 0.5 g of pre-synthesized EVMT powder were loaded into a 250 mL three-neck flask, followed by the addition of 100 mL oxygen-free deionized water under continuous stirring. Nitrogen was purged throughout the reaction to maintain an inert, oxygen-free atmosphere. A 1.0 mol/L NaOH solution was added drop-wise using a 100 mL constant-pressure dropping funnel until the solution pH reached 11, after which titration was terminated. The $FeSO_4{\cdot}7H_2O$ and $FeCl_3{\cdot}6H_2O$ with NaOH under heating to form Fe_3O_4 (Equation (1)), which is anchored on the surface of EVMT. The mixture was magnetically stirred at 60 °C in a water bath for 1 h. Upon completion of the reaction, the precipitate was rinsed repeatedly with distilled water to neutral pH. After drying in a vacuum oven at 80 °C for 6 h, the final Fe_3O_4@EVMT composite catalyst was obtained.

$$Fe^{2+} + 2Fe^{3+} + 8OH^{-} \xrightarrow{60\ ^{\circ}C,\ N_2} Fe_3O_4 \downarrow + 4H_2O \quad (1)$$

2.3. Characterization Techniques

Scanning electron microscopy (SEM, ZEISS Sigma 300) was utilized to observe the micromorphology of the samples. X-ray diffraction (XRD, Rigaku SmartLab SE, Cu K_α radiation $\lambda = 0.154$ nm; scanning range 5–80°; scanning speed 5° min^{-1}) was performed to identify the crystal structure. Nitrogen adsorption–desorption isotherm measurements were performed on a Micromeritics ASAP 2460 instrument (USA) to calculate the specific surface area of the as-prepared samples. The magnetic hysteresis loop was recorded at room temperature on a vibrating-sample magnetometer (LakeShore 7404). X-ray pho-

toelectron spectroscopy (XPS, Axis Supra) was employed to analyze the surface elemental composition of the catalyst. Surface functional groups were characterized via Fourier-transform infrared spectroscopy (FT-IR, Nicolet iS50), the spectra were recorded from 4000 to 400 cm^{-1}. Electron paramagnetic resonance (EPR, Bruker EMX-500 10/12) measurements were conducted to detect free-radical species generated in the reaction system.

2.4. Degradation Experiments

100 mL of pre-prepared MB solution (50 mg/L) was accurately transferred into a 250 mL beaker. Freshly prepared dilute HCl and NaOH solutions were used to adjust the initial pH. Predetermined amounts of the catalyst and H_2O_2 solution were added sequentially. The beaker was placed in a thermostatic shaker and shaken at a constant speed of 180 rpm under 25 °C. The filtrate was collected at reaction times of 0, 10, 20, 40, 60, 90, and 120 min, and the absorbance was measured at 659 nm using an ultraviolet-visible spectrophotometer, where the MB concentration was calculated accordingly. Single-factor batch experiments were performed to investigate the effects of pH, catalyst dosage and H_2O_2 concentration on MB removal efficiency, from which the optimal level for each factor was selected.

2.5. Reaction Kinetics

The pseudo-first-order (Equation (2)) and pseudo-second-order (Equation (3)) kinetic models were employed to fit the degradation data [18,19]. where C_0 and C_t (mg/L) are the initial MB concentration and the concentration at reaction time t, respectively, k_1 (min^{-1}) and k_2 (L/(mg · min)) represent the rate constants of the models.

$$\ln(C_t/C_0) = -k_1 t \quad (2)$$

$$1/C_t - 1/C_0 = k_2 t \quad (3)$$

2.6. Parameter Optimization (Response Surface Methodology)

Response surface methodology (RSM) combined with Box–Behnken Design (BBD) was utilized to evaluate the impacts of critical operational factors and their mutual interactions on the decomposition of MB within the Fe_3O_4@EVMT Fenton-like System. According to the outcomes of single-factor experiments, three independent factors including catalyst dosage, H_2O_2 concentration, and initial pH were investigated with three coded levels (−1, 0, +1). The response target was defined as the MB degradation efficiency (%). Table S1 lists the coded values and corresponding levels of all independent variables, the Design Expert 13.0 software was used for quadratic response surface regression analysis of the experimental data. A regression equation was constructed to carry out statistical analysis and prediction for the acquired experimental data.

3. Results

3.1. Characterization

Figure 1a shows that Fe_3O_4 nanoparticles exhibit a spherical morphology with relatively uniform particle size. Due to the high surface energy and interparticle magnetic attraction of nano-Fe_3O_4 particles, serious agglomeration readily occurs [20], whereby discrete Fe_3O_4 nanoparticles aggregate and assemble into large agglomerates. Figure 1b reveals that EVMT features a large skeletal structure, which offers sufficient space for the immobilization of Fe_3O_4 nanoparticles. Both EVMT and dispersed Fe_3O_4 particles can be

identified in Figure 1c, demonstrating that the Fe_3O_4@EVMT catalyst preserves the layered architecture of EVMT, accompanied by the inherent rough texture and partial pores of expanded vermiculite. The Fe_3O_4 nanoparticles are anchored on the EVMT surface rather than forming bulky agglomerates, which effectively suppresses particle aggregation and supplies abundant active sites for H_2O_2 activation. EDS results (Figure 1d) indicate that Fe_3O_4@EVMT mainly consists of Fe, O, Si, Mg and Al. Figure 1e displays the SEM micrograph of Fe_3O_4@EVMT after the degradation reaction. The catalyst morphology remains largely unchanged, while its surface turns rougher, the supported Fe_3O_4 nanoparticles agglomerate and grow in particle size. EDS elemental analysis (Figure 1f) identifies six elements on the used catalyst Fe, O, Si, Mg, Al and N. While N is the characteristic element of MB, confirming the adsorption of MB molecules on the catalyst surface, which agrees well with the following XPS results. The Fe content (wt%) of the catalyst decreases from 33.61% to 28.92% after reaction.

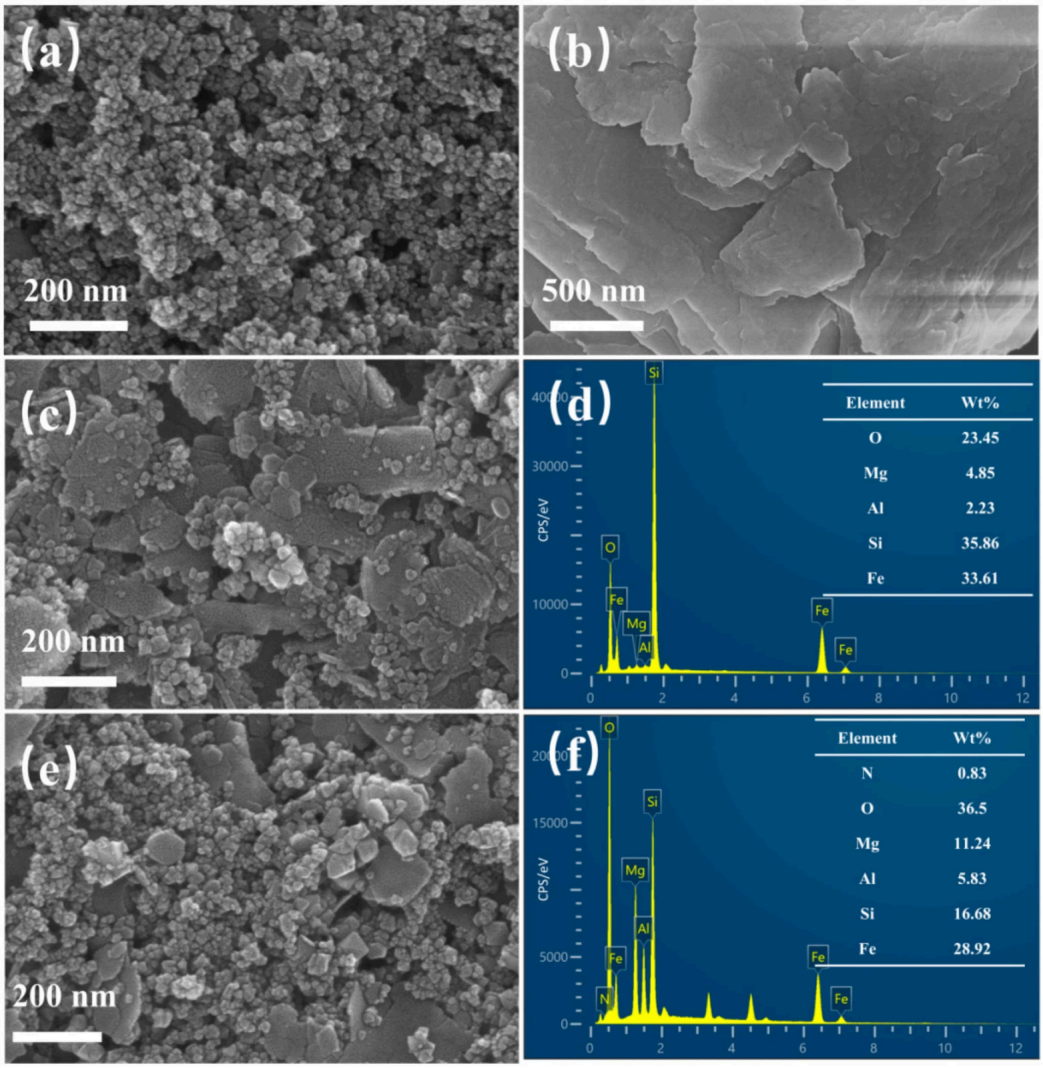


Figure 1. (**a**) Fe_3O_4; (**b**) EVMT; (**c**,**d**) Fe_3O_4@EVMT and its corresponding EDS spectrum; (**e**,**f**) Used Fe_3O_4@EVMT and its corresponding EDS spectrum.

As shown in Figure 2a, the Fe_3O_4@EVMT catalyst exhibits the characteristic peaks of EVMT at 7.6° and 26.4° (JCPDS 07-0042) [21]. Meanwhile, a set of sharp diffraction peaks emerge at 30.1°, 35.5°, 43.1°, 57.0° and 62.6°, matching the standard characteristic peaks of Fe_3O_4 [22]. This confirms the successful immobilization of Fe_3O_4 on the EVMT surface. According to the XRD results, the average crystallite size of supported Fe_3O_4 was

calculated to be 14.2 nm using the Scherrer equation based on the diffraction peak at 2θ of 35.5° [23]. The diffraction peak intensity of EVMT in Fe_3O_4@EVMT composite undergoes a slight reduction compared with the pure EVMT; however, the crystal structure of EVMT remains intact. Meanwhile, well-defined Fe_3O_4 diffraction peaks demonstrate that the crystalline structure of Fe_3O_4 is well-preserved upon loading.

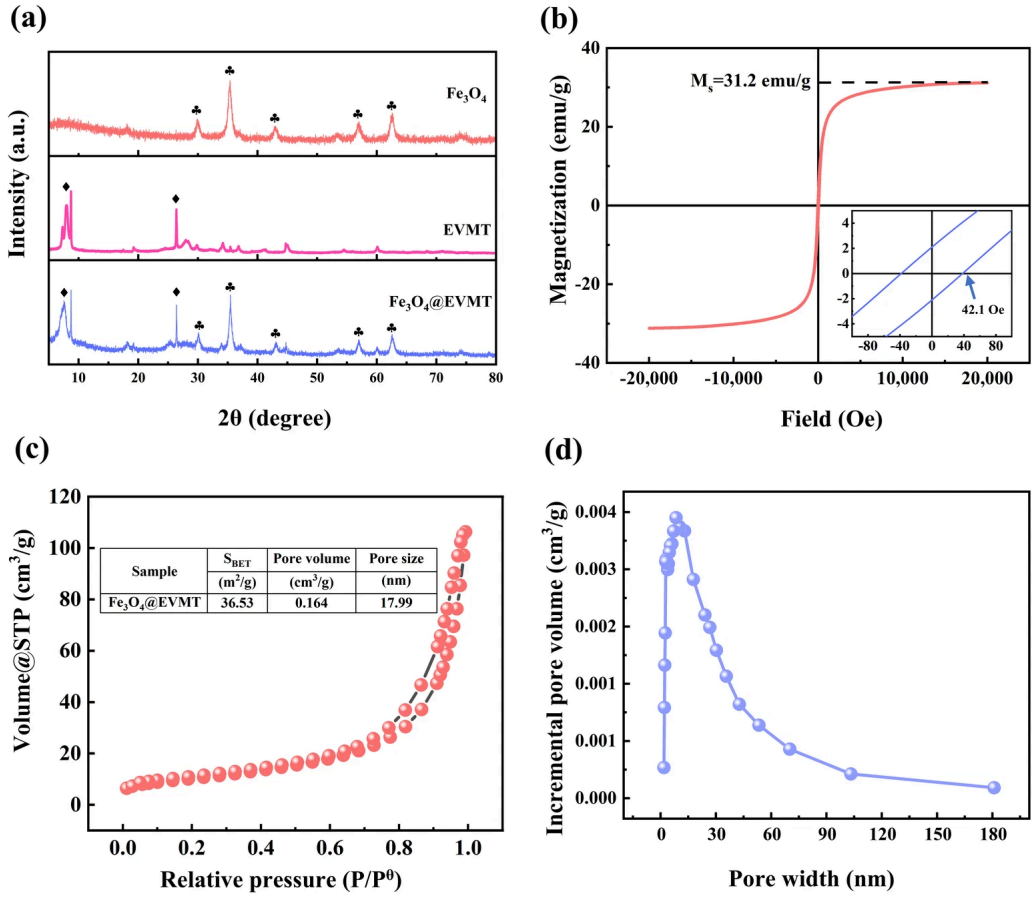


Figure 2. (**a**) XRD patterns of EVMT, Fe_3O_4, and Fe_3O_4@EVMT; (**b**) Magnetic hysteresis loop of Fe_3O_4@EVMT; (**c**) N_2 adsorption–desorption isotherms; (**d**) Pore diameter distribution.

The magnetic performance of Fe_3O_4@EVMT (Figure 2b) showed that the coercivity was 42.1 Oe, demonstrating that the synthesized material possessed ferromagnetic characteristics [24]. The saturation magnetization of Fe_3O_4@EVMT was 31.2 emu/g. The attenuation of magnetic saturation compared with the reported pure Fe_3O_4 [25] was mainly attributed to the introduction of non-magnetic EVMT substrate. Shikuku et al. [26] have reported a saturation magnetization of 6.22 emu/g for Fe_3O_4-supported kaolinite (Fe_3O_4@MC). The saturation magnetization of Fe_3O_4@EVMT in the present study is approximately five times that of the reported Fe_3O_4@MC. This difference may arise from variations in Fe_3O_4 loading, particle size, dispersion, and magnetic interactions associated with different mineral supports. The prepared Fe_3O_4@EVMT composite exhibited excellent magnetic responsiveness, allowing rapid solid–liquid separation under an external magnetic field.

The nitrogen adsorption–desorption isotherm (Figure 2c) and pore size distribution (Figure 2d) were employed to evaluate the surface and pore structural properties of Fe_3O_4@EVMT. The prepared composite possessed a high specific surface area of 36.53 m^2/g, an average pore size of 17.99 nm and a pore volume of 0.164 cm^3/g. The uniform

mesoporous structure and large specific surface area could effectively expose abundant surface active sites and accelerate mass transfer during the reaction process, thereby significantly improving the adsorption and catalytic degradation performance toward contaminants.

3.2. Effect of the Fe_3O_4/EVMT Mass Ratio

The degradation performance varied significantly with different Fe_3O_4/EVMT mass ratios in the catalyst. As shown in Figure 3a, the optimal degradation performance was achieved at a Fe_3O_4/EVMT mass ratio of 1:2. At this ratio, the EVMT support effectively dispersed Fe_3O_4 nanoparticles and prevented their aggregation, thereby maximizing the exposure of catalytic sites. The layered structure of EVMT also enriched MB around the catalyst surface, facilitating the contact between contaminants and reactive radicals. Excessive Fe_3O_4 led to particle agglomeration, while over-dosage of EVMT diluted active iron sites and reduced the generation of reactive oxygen species. Therefore, the Fe_3O_4@EVMT composite with Fe_3O_4/EVMT mass ratio of 1:2 was selected for subsequent experiments.

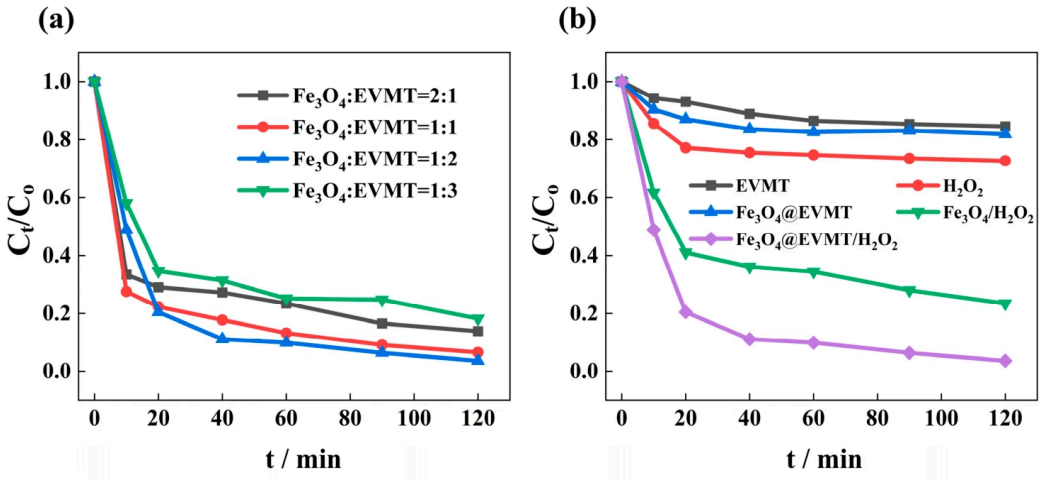


Figure 3. (**a**) The effect of the Fe_3O_4/EVMT mass ratio; (**b**) The MB removal efficiency in different systems ([MB] = 50 mg/L, pH = 4, [H_2O_2] = 5.0 mM, [catalyst] = 0.75 g/L, T = 25 °C).

3.3. Effect of Different Systems

As observed from Figure 3b, When EVMT, Fe_3O_4@EVMT and H_2O_2 were applied separately, their corresponding MB removal efficiencies reached 15.42%, 18.15% and 27.37%. Bare EVMT only relied on physical adsorption to capture MB without catalytic activity, leading to low pollutant removal. Without H_2O_2, Fe_3O_4@EVMT exhibited slightly higher adsorption capacity, yet no Fenton-like oxidation occurred. H_2O_2 alone showed limited oxidation capacity because it decomposed slowly to produce only a small amount of reactive radicals without a catalyst. The Fe_3O_4/H_2O_2 system achieved a degradation efficiency of 76.54%. Fe_3O_4 could activate H_2O_2 via the Fe^{2+}/Fe^{3+} redox cycle to generate active radicals for MB oxidation [27]. Surface-located Fe^{2+} sites on Fe_3O_4@EVMT react with H_2O_2 to produce hydroxyl radicals (·OH) and Fe^{3+}. Subsequently, the formed Fe^{3+} can be reduced back to Fe^{2+} through further reactions with H_2O_2, facilitating the regeneration of active iron sites. The generated reactive radicals attack the chromophore structure of MB molecules and promote the degradation of organic contaminants [28]. This cyclic iron redox process contributes to the high MB removal efficiency observed in our heterogeneous Fenton-like system. Nevertheless, severe aggregation of pure Fe_3O_4 nanoparticles reduced the exposure of active sites and in-

duced radical scavenging, which restricted the degradation performance. In contrast, the Fe_3O_4@EVMT/H_2O_2 system obtained the optimal MB removal of 96.43%. The layered EVMT support dispersed Fe_3O_4 nanoparticles effectively and alleviated particle agglomeration, greatly increasing accessible active sites. EVMT also enriched MB molecules near the catalyst surface, shortening the diffusion distance between contaminants and reactive radicals. The interfacial interaction between Fe_3O_4 and EVMT accelerated the Fe^{2+}/Fe^{3+} cycle and promoted H_2O_2 activation. Benefiting from the synergy of adsorption enrichment and interfacial Fenton-like catalysis, superior MB degradation was realized.

3.4. Effects of Parameters on MB Degradation

The effect of solution pH was presented in Figure 4a. The MB removal efficiencies of the Fe_3O_4@EVMT Fenton-like system were 88.31%, 96.43%, 84.62%, 48.57% and 30.16% at pH values of 2, 4, 6, 8 and 10, respectively. The maximum degradation efficiency was obtained at pH = 4. A degradation efficiency above 80% was maintained across a pH range of 2~6. Unlike conventional homogeneous Fenton reactions, which only function under strongly acidic environments, the Fe_3O_4@EVMT/H_2O_2 Fenton-like system extends the usable pH window. At pH = 2, excess H^+ ions could scavenge hydroxyl radicals and accelerates iron leaching, slightly impairing catalytic performance. When pH exceeded 4, rising OH^- facilitated the generation of ferric hydroxide precipitates on the catalyst surface, blocking active sites and inhibiting the Fe^{2+}/Fe^{3+} redox cycle. Under alkaline conditions (pH = 8 and 10), H_2O_2 preferentially underwent ineffective decomposition instead of producing ·OH [29]. Meanwhile, the surface charge of the catalyst altered, weakening its adsorption capacity for cationic MB. Consequently, the degradation efficiency declined markedly as pH increased. Accordingly, pH 4 was selected for the subsequent Box–Behnken experimental design.

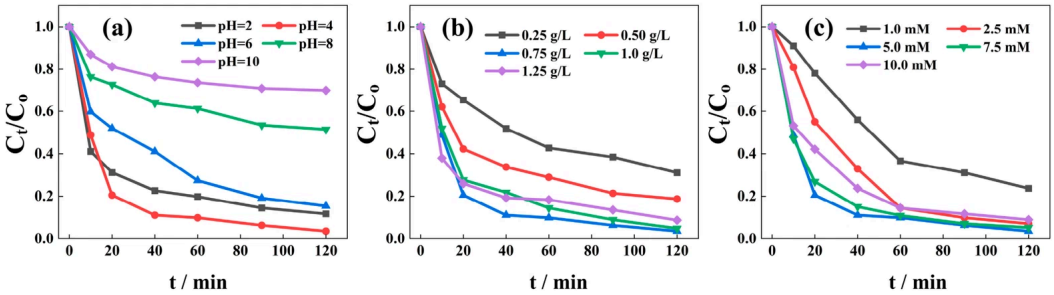


Figure 4. Effect of (**a**) pH, (**b**) catalyst dosage and (**c**) H_2O_2 dosage ([MB] = 50 mg/L, T = 25 °C).

Figure 4b illustrates the effect of catalyst dosage. The MB removal efficiencies of the Fe_3O_4@EVMT/H_2O_2 Fenton-like system were 68.95%, 81.32%, 96.43%, 95.14% and 91.27% at catalyst dosages of 0.25, 0.50, 0.75, 1.00 and 1.25 g/L, respectively. The optimal degradation performance was achieved at a catalyst dosage of 0.75 g/L. At low dosages (0.25 and 0.5 g/L), the number of accessible active sites was insufficient, restricting the generation of active radicals and resulting in low MB removal efficiency. Raising the catalyst dosage to 0.75 g/L provided abundant active sites to activate H_2O_2, producing sufficient ·OH for MB oxidation and thereby yielding the maximum removal efficiency. A further increase in dosage to 1.0 and 1.25 g/L led to a slight reduction in degradation performance. Excess catalyst triggered radical scavenging, where ·OH radicals were depleted prior to reaction with MB ($Fe^{2+} + ·OH \rightarrow Fe^{3+} + OH^-$). Meanwhile, particle agglomeration took place at high solid loading, shielding part of the active sites [30]. Excessive iron sites also accelerated the ineffective decomposition of H_2O_2, further decreasing the yield of reactive radicals for pollutant degradation. Hence, 0.75 g/L was selected as the catalyst

dosage for the subsequent Box–Behnken experimental design.

Figure 4c depicts the influence of H_2O_2 dosage on MB degradation. The degradation efficiency rose first and then declined with increasing H_2O_2 concentration, and the maximum degradation efficiency was achieved at an H_2O_2 dosage of 5 mmol/L. Increasing the H_2O_2 dosage to 5.0 mmol/L provided sufficient precursor to produce abundant ·OH via catalytic activation, achieving the highest MB degradation efficiency. A further rise in H_2O_2 dosage to 7.5 and 10 mmol/L induced a slight decrease in degradation performance. Excess H_2O_2 acted as a scavenger of ·OH radicals through the reaction (H_2O_2 + ·OH → HO_2· + H_2O). The formed hydroperoxyl radicals (HO_2·) exhibit much weaker oxidation capacity than ·OH [31]. Meanwhile, excess H_2O_2 competed for active sites on the catalyst surface, inhibiting the effective activation of H_2O_2 and reducing the concentration of available reactive radicals for pollutant degradation. Therefore, 5.0 mmol/L was selected as the optimal H_2O_2 dosage for the subsequent Box–Behnken experimental design.

3.5. Optimization of the Process

The experimental data acquired from the 17 test runs are listed in Table S2, and the second-order polynomial model of response surface methodology was developed for the Fe_3O_4@EVMT/H_2O_2 Fenton-like system as follows:

Removal rate (%) = 96.66 − 1.86A + 2.31B − 1.17C − 0.4375AB − 0.0675AC + 1.83BC − 12.45A^2 + 0.3908B^2 − 2.28C^2 (A, B, and C represent the coded values of initial pH, catalyst dosage, and H_2O_2 concentration, respectively).

The analysis of variance (ANOVA) was performed to evaluate the statistical significance of the developed quadratic response surface model, and the results are summarized in Table S3. The model presents an F-value of 115.40 with a *p*-value below 0.0001, indicating that the regression model is highly significant [32]. The coefficient of determination (R^2 = 0.9933) demonstrates that the model can explain approximately 99.33% of the variance in MB degradation efficiency. The adjusted R^2 (0.9847) is in reasonable agreement with the predicted R^2 (0.9268), with a difference of less than 0.2. The coefficient of variation (C.V. = 0.97%) and the standard deviation (0.8697) are both low, reflecting the high precision and reliability of the experimental data. The adequate precision value of 28.35 far exceeds the desirable threshold of 4, indicating an adequate signal-to-noise ratio. Moreover, the lack-of-fit term is not significant (F = 2.46, p = 0.2019 > 0.05), confirming that the quadratic model adequately fits the experimental data [33].

The linear terms A (pH, p = 0.0005), B (catalyst dosage, p = 0.0001) and C (H_2O_2 concentration, p = 0.0067) are all statistically significant. Among the quadratic terms, A^2 (p < 0.0001) and C^2 (p = 0.0010) are extremely significant, whereas B^2 is insignificant (p = 0.3873). Notably, A^2 exhibits the largest F-value (863.39), demonstrating that the quadratic effect of pH overwhelmingly dominates the response. For the interaction terms, only BC (catalyst dosage × H_2O_2 concentration, p = 0.0040) is statistically significant, while AB (p = 0.3479) and AC (p = 0.8810) are not significant. Based on the F-values, the order of factor influence on MB degradation efficiency is: A^2 > B > A > C^2 > BC > C > AB > B^2 > AC.

A set of diagnostic plots was generated to evaluate the predictive performance of the model on MB degradation efficiency. Figure 5a illustrates the correspondence between predicted and observed responses for MB degradation. The data points lie close to the regression line, indicating good consistency between the empirical model and experimental measurements. The normal probability plot of studentized residuals shows that residuals follow a normal distribution (Figure 5b), providing additional evidence to support the model's reliability [34].

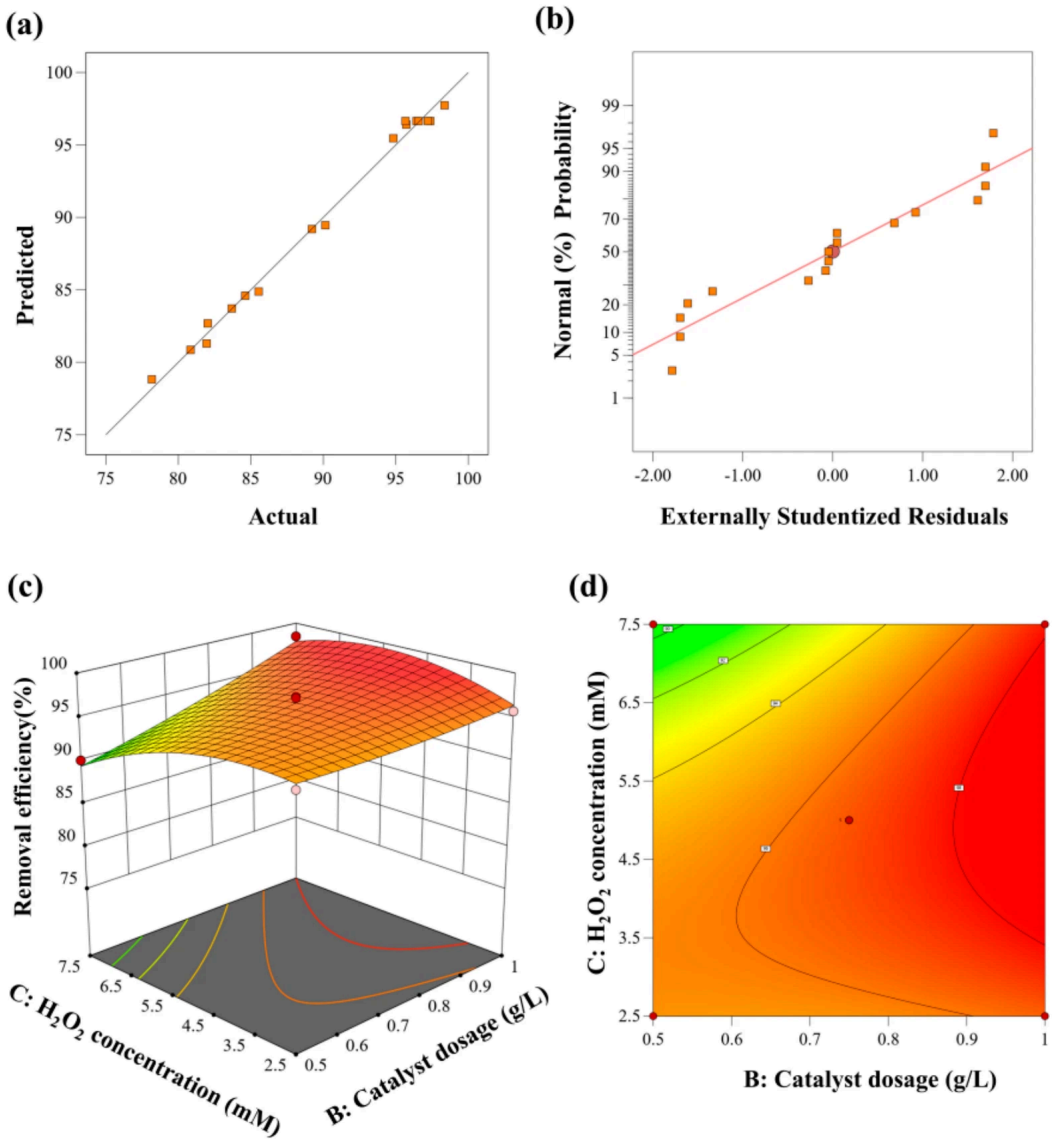


Figure 5. (**a**) Plot of experimental values versus predicted values; (**b**) normal probability plot of standardized residuals for the removal efficiency; interactive influence between catalyst dosage and H_2O_2 concentration; (**c**) 3D response surface plot; (**d**) 2D contour plots.

As only the interaction between catalyst dosage and H_2O_2 concentration (B × C) exerted a significant impact on MB degradation, Figure 5c,d presents the 3D response surface plot and corresponding 2D contour plots to describe the relationship between these two factors. The variation trend of removal efficiency agreed well with the findings from single-factor experiments. The elliptical contour lines further verified the strong interactive effect of catalyst dosage and H_2O_2 concentration.

Figure S1 displays the 3D response surface plot for the interaction between pH and catalyst dosage (A × B). The contour lines were nearly parallel rather than elliptical, demonstrating a negligible interaction between these two variables. At a fixed catalyst dosage, the MB removal efficiency first increased and then decreased with rising pH, achieving the optimal performance within the pH range of 3~4. These observations indicated that pH and catalyst dosage independently governed the MB degradation performance.

Figure S2 also shows the 3D response surface plot for the interaction between pH and H_2O_2 concentration (A × C). At a given pH value, the removal efficiency first increased and then slightly declined as the H_2O_2 concentration increased. Although the

contour lines exhibited an elliptical shape, the ANOVA results confirmed that the interactive effect between pH and H_2O_2 concentration was insignificant. This finding demonstrates that pH and H_2O_2 concentration independently controlled the MB degradation performance in the Fe_3O_4@EVMT Fenton-like system.

3.6. Model Validation Test

Response surface optimization was applied to determine the optimal reaction conditions, which yielded a maximum predicted degradation efficiency of 98.934%. The predicted optimum conditions were as follows: catalyst dosage of 0.974 g/L, H_2O_2 concentration of 4.485 mmol/L, and initial pH of 3.774. To verify the reliability of these predicted results, validation experiments were conducted. Considering the feasibility of practical operation, the optimal parameters were moderately adjusted to pH = 3.8, catalyst dosage = 1.0 g/L, and H_2O_2 dosage = 4.5 mmol/L. Three parallel validation tests were performed under these modified conditions (Figure 6a). The average MB removal efficiency reached 98.26%, with a minor deviation relative to the model prediction. This finding confirms that the established response surface model is accurate and reliable for reaction parameter optimization. Kinetic fitting analysis was further conducted on the experimental data, and the fitting results are displayed in Figure 6b,c. The pseudo-second-order kinetic model exhibited higher correlation coefficients (R^2) than the pseudo-first-order kinetic model, demonstrating that the MB degradation process by the Fe_3O_4@EVMT Fenton-like system follows pseudo-second-order reaction kinetics. Accordingly, chemical reaction serves as the dominant factor throughout the degradation process [35].

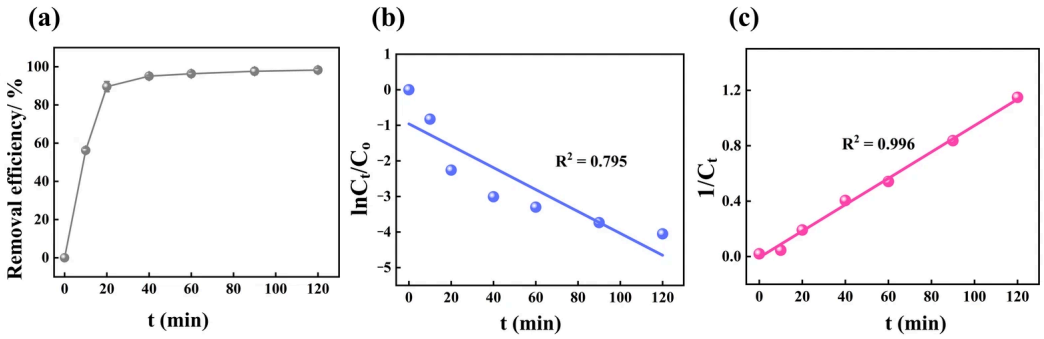


Figure 6. (**a**) Variation in removal efficiency over time ([MB] = 50 mg/L, pH = 3.8, [H_2O_2] = 4.5 mM, [catalyst] = 1.0 g/L, T = 25 °C); (**b**) Fitting plot of pseudo-first-order kinetics; (**c**) Fitting plot of pseudo-second-order kinetics.

3.7. Effect of Temperature

Figure 7a illustrates the MB removal efficiency of the Fe_3O_4@EVMT Fenton-like system at 25, 35 and 45 °C, with degradation efficiencies consistently exceeding 98%. Kinetic fitting confirms that the degradation follows the pseudo-second-order kinetic model, and the corresponding rate constants of k_2 rise gradually with increasing temperature (Figure 7b). In accordance with previous reports, the Arrhenius equation ($\ln k = -E_a/(RT) + \ln A_0$) enables the calculation of activation energy (E_a) [36,37]. In this work, k_2 was substituted for the apparent rate constant k in Arrhenius equation; A_0 is defined as the pre-exponential factor. The linear fitting of ln k_2 against 1/T is shown in Figure 7c, yielding an E_a of 40.2 kJ/mol from the regression slope. Such a relatively high activation energy originates from the requirement to surmount energy barriers and break chemical bonds of substrate molecules during the Fenton-like oxidation reaction.

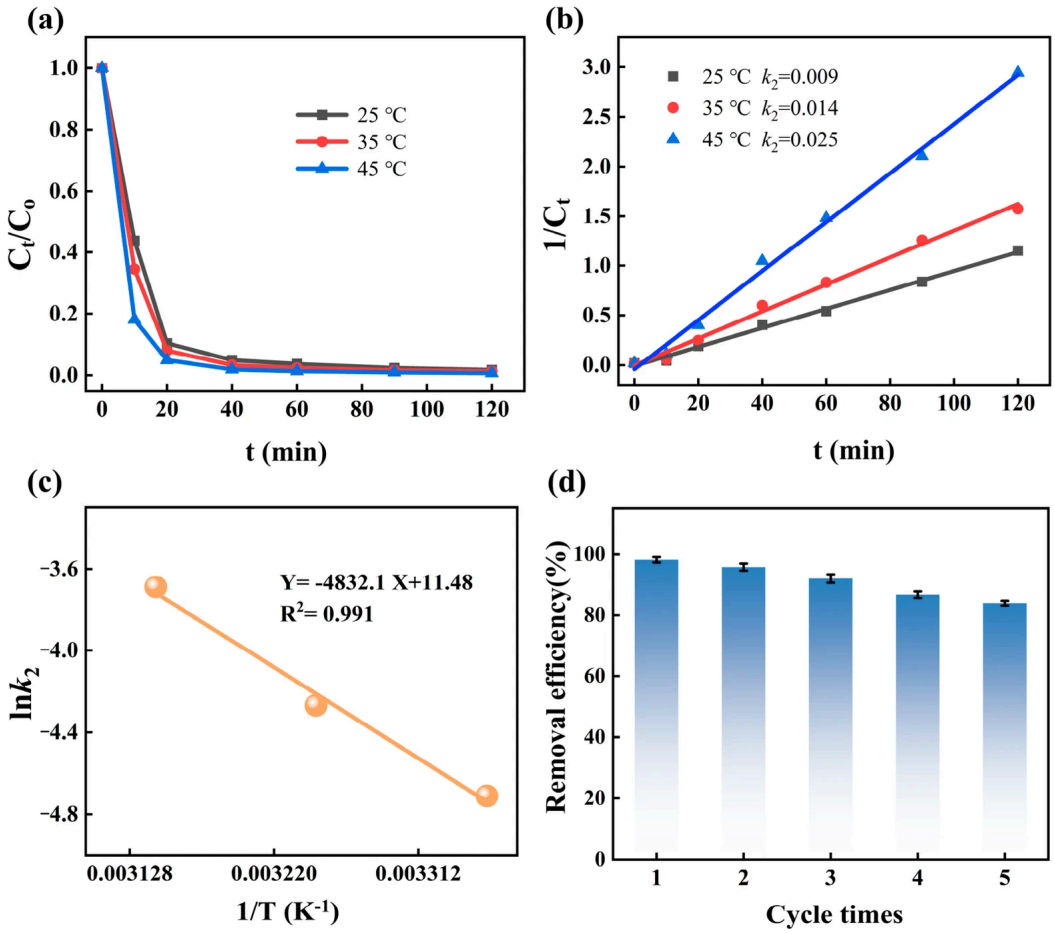


Figure 7. (**a**) Influence of temperature; (**b**) Fitting plots of pseudo-second-order kinetics; (**c**) Arrhenius linear fitting; (**d**) Catalyst recycling experiments ([MB] = 50 mg/L, pH = 3.8, [H_2O_2] = 4.5 mM, [catalyst] = 1.0 g/L).

3.8. Reusability Performance

After each degradation experiment, the Fe_3O_4@EVMT catalyst was separated and recycled via magnetic attraction. The recovered solid catalyst was rinsed alternately with oxygen-free deionized water and ethanol, then dried in a vacuum oven. As shown in Figure 7d, the MB degradation efficiency gradually declined upon successive cycling runs. This observation is primarily ascribed to the loss of immobilized Fe_3O_4 nanoparticles during repeated reactions, as well as the incomplete desorption of residual MB molecules adsorbed on the catalyst surface [38]. Remarkably, the catalyst retained an MB removal efficiency of 83.9% after five consecutive cycles, which confirms its satisfactory reusability.

3.9. Mechanism Analysis

3.9.1. Water Contact Angle Test, FTIR and XRD Characterization After Reaction

Figure 8a shows that the water contact angle of bare Fe_3O_4 nanoparticles was measured to be 33.9°, revealing its hydrophilic property. After immobilizing Fe_3O_4 onto EVMT, the contact angle of the Fe_3O_4@EVMT composite decreased to 23.8°, demonstrating enhanced surface hydrophilicity. This improvement is attributed to abundant polar hydroxyl groups on the EVMT skeleton. The layered porous structure of EVMT together with enriched surface hydrophilic groups facilitates water spreading on the catalyst surface. Such favorable hydrophilicity promotes the diffusion and contact of MB molecules in aqueous solution with the active sites of the catalyst, which is beneficial to the Fenton-

like degradation reaction.

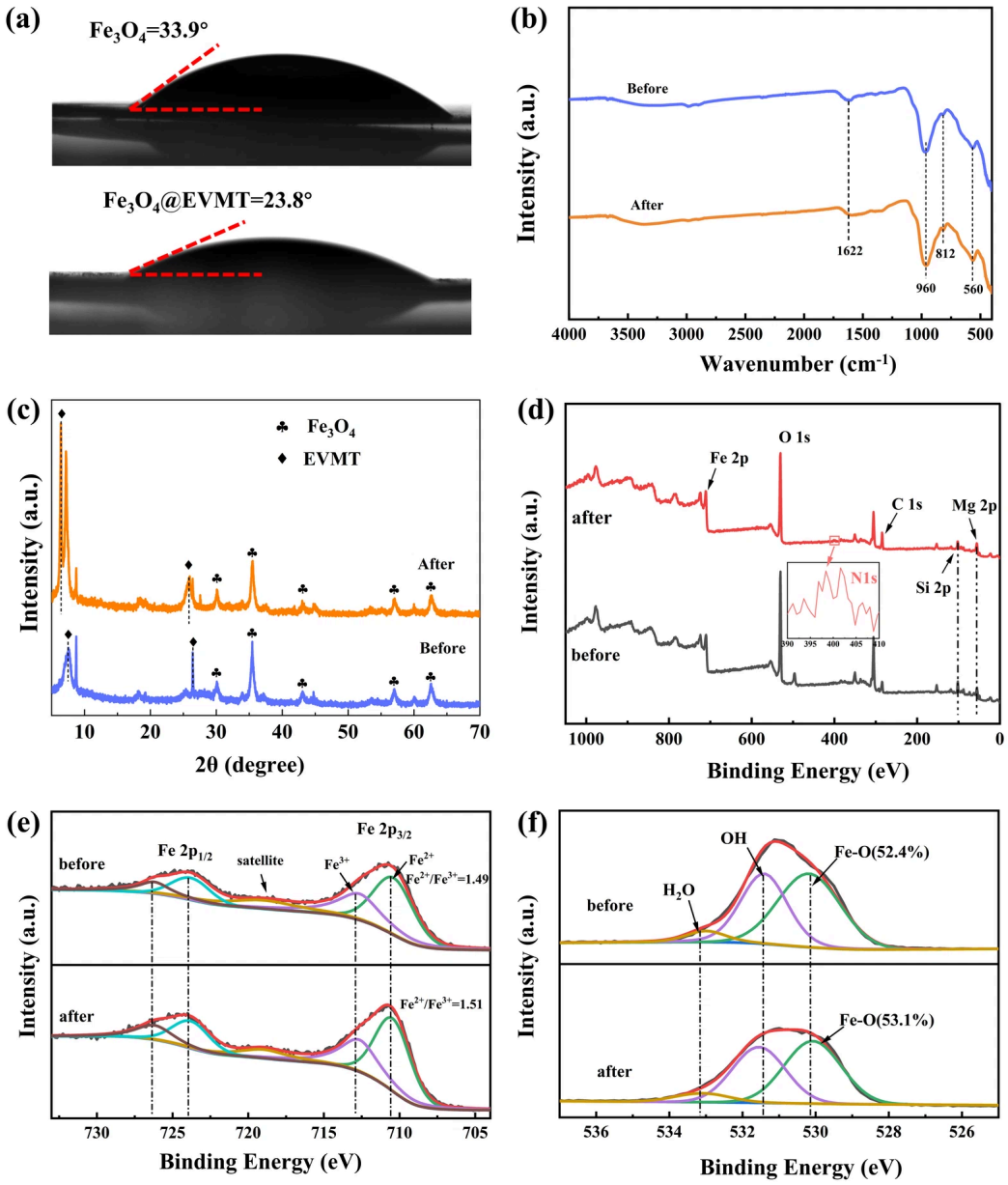


Figure 8. (**a**) Water contact angle of Fe_3O_4 and Fe_3O_4@EVMT; (**b**) FTIR spectra and (**c**) XRD pattern of Fe_3O_4@EVMT before and after reaction; XPS spectra of (**d**) Fe_3O_4@EVMT; (**e**) Fe 2p; (**f**) O 1s.

As depicted in Figure 8b, the absorption peak at 1622 cm^{-1} corresponds to the O–H bending vibration of surface-adsorbed water [39]. The characteristic peaks at 960 and 812 cm^{-1} are attributed to the Si–O–Si stretching vibration of EVMT, whereas the band at 560 cm^{-1} originates from the Fe–O stretching vibration of Fe_3O_4 [40]. No obvious shift or disappearance of these characteristic peaks can be detected after degradation, which confirms the structural stability of the Fe_3O_4@EVMT catalyst. Figure 8c presents the XRD patterns of Fe_3O_4@EVMT exhibit no significant variations after the reaction. The characteristic diffraction peaks of Fe_3O_4 remain intact. By contrast, the EVMT characteristic peaks at 7.6° and 26.4° shifted toward lower angles, indicating expanded interlayer spacing of EVMT [41]. This observation implies that MB molecules were intercalated into the interlayer of EVMT. Collectively, the layered framework of EVMT and the active crys-

talline phase of Fe_3O_4 were well retained throughout the Fenton-like reaction, further verifying the favorable structural stability of the catalyst.

3.9.2. XPS Characterization

The XPS survey spectrum (Figure 8d) reveals that Fe_3O_4@EVMT mainly consists of Mg, Fe, O, C and Si, which matches the EDS results. A weak N 1s signal emerged near 400 eV after the degradation, verifying the adsorption of MB molecules onto the catalyst surface. For the Fe 2p spectrum (Figure 8e), the characteristic peaks at 710.6 eV and 712.9 eV are assigned to Fe^{2+} and Fe^{3+}, respectively [42,43]. The Fe^{2+}/Fe^{3+} peak area ratio was 1.49 before reaction and slightly rose to 1.51 after the reaction. This negligible change demonstrates that the valence distribution of iron species was well preserved, and the intrinsic structure of Fe_3O_4 was not damaged during the catalytic process. As displayed in the O 1s spectrum (Figure 8f), the peak at 530.1 eV originates from Fe–O bonding [44]. The relative peak area of Fe–O slightly increased from 52.4% to 53.1% after degradation, which can be attributed to the in situ formation of iron oxides during catalytic oxidation. The signals at 531.4 eV and 533.2 eV correspond to surface –OH groups and adsorbed water molecules, respectively. Such minor variation in the Fe–O peak fraction further confirms that the surface chemical state of iron species barely altered after the Fenton-like reaction, which is in good accordance with the foregoing XRD and FTIR results.

3.9.3. Analysis of Reactive Active Species

Tertiary butanol (TBA) and benzoquinone (BQ) were used as scavengers for ·OH and $\cdot O_2^-$, respectively. As illustrated in Figure 9a, the MB removal efficiency dropped drastically to 26.4% upon the addition of 5 mmol/L TBA for ·OH quenching. By comparison, introducing 5 mmol/L BQ to trap $\cdot O_2^-$ exerted a negligible inhibitory influence, with the removal efficiency retaining 92.1%. These observations demonstrate that $\cdot O_2^-$ was not the dominant reactive species for MB degradation. Full-wavelength scanning was carried out for filtrate samples collected at different reaction times (Figure 9b). The MB solution exhibited three characteristic absorption peaks within the 200~800 nm range, among which the maximum peak at 659 nm was assigned to the monomer of MB. The absorbance intensity gradually declined as the reaction proceeded, revealing the efficient destruction of chromophore groups in MB molecules [45]. Moreover, the variation in dissolved iron concentration in the Fe_3O_4@EVMT/H_2O_2 system was tracked throughout the reaction. As shown in Figure 9c, the total dissolved iron concentration remained as low as 0.24 mg/L during the whole degradation process, which suggests only a minor portion of Fe_3O_4 leached from the catalyst. This finding further confirms the outstanding structural stability of Fe_3O_4@EVMT, and the catalytic reaction mainly proceeds at the solid–liquid interface [46]. Electron spin resonance signals of ·OH and $\cdot O_2^-$ were captured after 10 min of reaction (Figure 9d), verifying that the Fe_3O_4@EVMT catalyst can activate H_2O_2 to produce both ·OH and $\cdot O_2^-$ reactive radicals [47]. In particular, the signal intensity of ·OH was markedly stronger, suggesting that ·OH plays a major role in MB removal, whereas $\cdot O_2^-$ may make a relatively minor contribution under the investigated conditions.

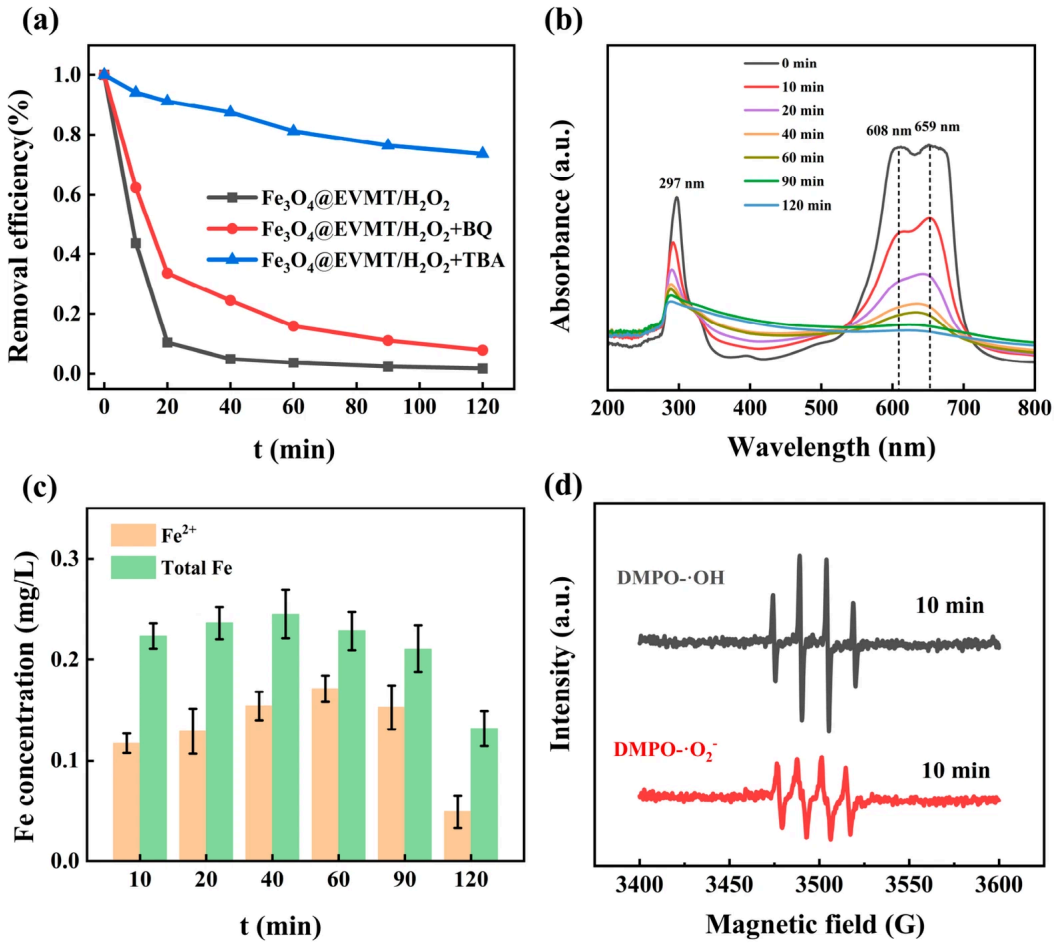


Figure 9. (**a**) Free radical trapping experiments; (**b**) UV-Vis full wavelength scan during MB degradation; (**c**) variation of iron concentrations; (**d**) electron spin resonance spectra of free radicals captured by DMPO ([MB] = 50 mg/L, pH = 3.8, [H_2O_2] = 4.5 mM, [catalyst] = 1.0 g/L, T = 25 °C).

4. Conclusions

In this study, a high-efficiency heterogeneous Fenton-like catalyst (Fe_3O_4@EVMT) was successfully synthesized by immobilizing nano Fe_3O_4 particles on EVMT. XRD, SEM-EDS and XPS characterisation confirmed that the Fe_3O_4 nanoparticles were deposited on the external surfaces of the layered EVMT, and that the severe agglomeration of bare magnetite was effectively suppressed after immobilization; the composite retained superparamagnetic behaviour with a saturation magnetization of 31.2 emu/g, which enabled rapid magnetic recovery by an external magnet. The constructed Fe_3O_4@EVMT/H_2O_2 Fenton-like system exhibited outstanding catalytic performance for the degradation of MB in aqueous solution. Under the optimized conditions of pH 3.8, catalyst dosage 1.0 g/L and H_2O_2 concentration 4.5 mmol/L, the MB removal efficiency reached 98.26%, in good agreement with the value predicted by the model. Box–Behnken response surface methodology was employed to systematically optimize the key operational parameters. Response surface analysis indicated that solution pH, catalyst dosage, and H_2O_2 concentration significantly affected MB removal efficiency. Among the interaction terms, only the interaction between catalyst dosage and H_2O_2 concentration was statistically significant (p = 0.0040), whereas the interactions involving solution pH were not significant (p > 0.05). The quadratic regression model was highly significant (p < 0.0001), with an R^2 value of 0.9933, verifying the accuracy and reliability of the predictive equation. The adequate signal-to-noise ratio of 28.35 and the insignificant lack-of-fit term (F = 2.46, p = 0.2019) further confirmed the adequacy of the quadratic

model, and the quadratic term of pH (A^2, F = 863.39) was identified as the factor dominating the response. Cycling stability tests demonstrated that the catalyst retained an MB removal efficiency of over 80% after five consecutive cycles, confirming its favorable reusability and operational stability. In addition, the dissolved iron concentration in the reaction liquor remained low (below 0.24 mg/L) throughout the reaction, and XRD, XPS and FTIR analyses of the spent catalyst showed that both the host structure and the Fe^{2+}/Fe^{3+} ratio were essentially preserved. Kinetic fitting results indicated that the MB degradation process confirmed the validity of the pseudo-second-order kinetic model, and the activation energy of the catalytic reaction was calculated to be 40.2 kJ/mol. This finding further validated that chemical oxidation dominated the MB removal mechanism in this Fenton-like system. Furthermore, the proposed catalytic strategy possesses prominent advantages, including a simple process flow and convenient operational control; further experiments employing multiple contaminants (anionic dyes, antibiotics) and real industrial wastewater are required to better assess the general applicability of the catalyst in practical water treatment scenarios.

Supplementary Materials: The following supporting information can be downloaded at https://www.mdpi.com/article/doi/s1, Table S1: Experimental level for Box–Behnken design; Table S2: Experimental matrix by Box–Behnken design and actual and predicted responses; Table S3: ANOVA results of quadratic model for MB degradation; Figure S1: Interactive influence between catalyst dosage and pH (a) 3D response surface plot, (b) 2D contour plots; Figure S2: Interactive influence between H_2O_2 concentration and pH (a) 3D response surface plot, (b) 2D contour plots.

Author Contributions: Y.Z.: investigation, methodology, writing—original draft. X.Y.: writing—review and editing, investigation, data curation. X.H.: methodology, formal analysis. W.W.: formal analysis, resources. D.S.: resources, writing—review and editing. H.T.: resources, funding acquisition, writing—review and editing. All authors have read and agreed to the published version of the manuscript.

Funding: This research was funded by Scientific Research Project of Kashi University (20232851); Key-Area Research and Development Program of Guangdong Province (2024B0202010001); The presidential research fund of Tarim University (TDZKSS202127).

Institutional Review Board Statement: Not applicable.

Informed Consent Statement: Not applicable.

Data Availability Statement: The data presented in this study are available on request from the corresponding author.

Conflicts of Interest: The authors declare no conflicts of interest.

References

1. Wang, H.; Chen, W.; Yan, S.; Guo, C.; Ma, W.; Yang, A. Zirconium-doped MCM-41 from zirconium-containing silica residue for methylene blue removal: One-pot hydrothermal synthesis, characterization, and dye adsorption performance. *Sep. Purif. Technol.* **2025**, *376*, 133961. [Google Scholar] [CrossRef]
2. Liu, Z.; Khan, T.A.; Islam, M.A.; Tabrez, U. A review on the treatment of dyes in printing and dyeing wastewater by plant biomass carbon. *Bioresour. Technol.* **2022**, *354*, 127168. [Google Scholar] [CrossRef] [PubMed]
3. Mishra, S.R.; Mandal, T.; Kumar, P.; Verma, V.; Senapati, R.N.; Kumar, M.; Singh, V. Microporous activated carbon from Madhuca longifolia flower for efficient methylene blue dye removal in wastewater treatment. *Surf. Interfaces* **2025**, *69*, 106770. [Google Scholar] [CrossRef]
4. Bugarcic, M.; Velickovic, Z.; Radovanovic, Z.; Milosevic, M.; Mijatov, S.; Stojanovic, J.; Marinkovic, A. Phyllosilicate-based adsorbents decorated with iron oxyhydroxides: Application for lead, chromates and selenites removal. *Sci. Sinter.* **2024**, *56*, 485–503. [Google Scholar] [CrossRef]

5. Ahmed, H.R.; Kayani, K.F. A comparative review of Fenton-like processes and advanced oxidation processes for methylene blue degradation. *Inorg. Chem. Commun.* **2024**, *170*, 113467. [Google Scholar] [CrossRef]
6. Wang, M.; Yang, F.; Yuan, Y.; Xing, C.; Wang, H.; Liu, Y.; Sun, Y.; Guan, X. Enhanced Fenton-like treatment of real leather wastewater using sulfidated zero-valent iron: Performance, mechanism, and phosphorus recovery. *Water Res.* **2026**, *308*, 126923. [Google Scholar] [CrossRef] [PubMed]
7. Daher, E.A.; Al Redda, A.; Laberty-Robert, C.; Hamd, W. Design of a new ZnO photocatalytic Fenton-like system for enhancing the removal of methylene blue at neutral pH. *Ceram. Int.* **2024**, *50*, 20843–20850. [Google Scholar] [CrossRef]
8. Niu, Y.; Wang, W.; Zhao, M.; Wang, N.; Jensen, M.; Han, N.; Li, X. Fe_3O_4-doped DCD-modified PAN-based nanofiber mat with synergistic photo-Fenton catalytic evaporation performance for multifaceted water treatment. *J. Environ. Chem. Eng.* **2026**, *14*, 122793. [Google Scholar] [CrossRef]
9. Liang, X.; Li, L.; Wu, Y.; Liu, F.; Wang, Y.; Wu, Y. Cu-doped Fe_3O_4 coupled to MIL-101(Fe) for the preparation of composites with enhanced photo-Fenton degradation of tetracycline hydrochloride. *J. Water Process Eng.* **2025**, *73*, 107698. [Google Scholar] [CrossRef]
10. Martínez-Costa, J.I.; Rivera-Utrilla, J.; Leyva-Ramos, R.; Sánchez-Polo, M.; Velo-Gala, I. Individual and simultaneous degradation of antibiotics sulfamethoxazole and trimethoprim by UV and solar radiation in aqueous solution using bentonite and vermiculite as photocatalysts. *Appl. Clay Sci.* **2018**, *160*, 217–225. [Google Scholar] [CrossRef]
11. Gülbiçim, H.; Tufan, M.Ç.; Türkan, M.N. The investigation of vermiculite as an alternating shielding material for gamma rays. *Radiat. Phys. Chem.* **2017**, *130*, 112–117. [Google Scholar] [CrossRef]
12. Zhu, J.; Sun, M.; Ren, Y.; Yao, J.; Cao, J.; Zhang, J. Cotton shell biomass–derived carbon–supported Fe_2O_3/Fe_3O_4 nanohybrids for efficient oxygen evolution reaction. *Fuel* **2026**, *406*, 136903. [Google Scholar] [CrossRef]
13. Eldos, H.I.; Khan, M.; Zouari, N.; Saeed, S.; Al-Ghouti, M.A. Adsorptive removal of volatile petroleum hydrocarbons from aqueous solution by zeolite imidazole framework (ZIF-8) and iron oxide (Fe_3O_4) nanoparticles. *Environ. Technol. Innov.* **2023**, *32*, 103382. [Google Scholar] [CrossRef]
14. Tomczyk, A.; Sokołowska, Z.; Boguta, P. Biochar physicochemical properties: Pyrolysis temperature and feedstock kind effects. *Rev. Environ. Sci. Biotechnol.* **2020**, *19*, 191–215. [Google Scholar] [CrossRef]
15. Salhi, M.; Louzri, S. Synthesis and characterization of a layered double hydroxide as a novel, stable, and regenerable electrocatalyst for methylene blue elimination. *Appl. Clay Sci.* **2025**, *265*, 107679. [Google Scholar] [CrossRef]
16. Eltaweil, A.S.; Al Harby, N.; El Batouti, M.; Pasam, G.; Al Kitani, M.; Abd El Monaem, E.M. Magnetic algae-derived $FeS_{0.66}$@GA-$BC_{0.33}$ composite for Cr(VI) removal optimized by response surface methodology. *Mater. Chem. Phys.* **2026**, *364*, 132792. [Google Scholar] [CrossRef]
17. Syahputri, Y.; Gunlazuardi, J.; Zulys, A. Synthesis of samarium-MOFs and their application for photocatalytic hydrogen production with Box-Behnken response surface methodology for performance optimization. *Vacuum* **2026**, *253*, 115581. [Google Scholar] [CrossRef]
18. Hu, J.; Hu, P. Evaluation of a novel kaolinite loaded sulfidized nZVI aggregates for removing Cr(VI) and Cd(II) in water: New sulfurization strategy, morphological control, performance, and synergistic mechanisms. *Sep. Purif. Technol.* **2025**, *363*, 132171. [Google Scholar] [CrossRef]
19. Zhao, D.; Liu, Y.; Wu, C. Adsorption of Cr(VI) polluted water by Fe_3O_4@SiO_2-APTMS nanocomposites prepared in the presence of ultrasonic irradiation for sustainable water resources utilization. *Ultrason. Sonochem.* **2023**, *96*, 106439. [Google Scholar] [CrossRef] [PubMed]
20. Sun, H.; Wang, L.; Wang, X.; Dong, Y.; Xin, J.; Ren, J.; An, J.; Jing, R. Construction of recyclable magnetic PEI-modified GO/Fe_3O_4 adsorbents for high-efficient removal of Cr(VI) ions from aqueous solutions. *Solid State Sci.* **2024**, *154*, 107611. [Google Scholar] [CrossRef]
21. Shen, Y.W.; Bian, J.; Wang, Y.B.; Yang, X.Y.; Tian, W.L. Continuous microwave tunnel expansion of vermiculite: A comparative study with thermal/chemical methods for structure-intact performance enhancement. *RSC Adv.* **2025**, *15*, 35047–35054. [Google Scholar] [CrossRef] [PubMed]
22. Chen, H.; Xu, J.; Shi, J.; Zhang, Z.; Zhaludkevich, A.L.; Liu, X.; Yang, Y. Magnetic nanoparticles mediate interface engineering for ultralow-loss FeSiBCuNb/Fe_3O_4 soft magnetic composites via thermal decomposition. *Adv. Powder Technol.* **2026**, *37*, 105366. [Google Scholar] [CrossRef]
23. Falyouna, O.; Bensaida, K.; Maamoun, I.; Ashik, U.P.M.; Tahara, A.; Tanaka, K.; Aoyagi, N.; Sugihara, Y.; Eljamal, O. Synthesis of hybrid magnesium hydroxide/magnesium oxide nanorods [$Mg(OH)_2$/MgO] for prompt and efficient adsorption of

ciprofloxacin from aqueous solutions. *J. Clean. Prod.* **2022**, *342*, 130949. [Google Scholar] [CrossRef]
24. Yang, X.; Dai, X.; Jian, T.; Tian, W. Enhanced adsorption and reduction of Pb(II) from aqueous solution by sulfide-modified nanoscale zerovalent iron: Characterization, kinetics and mechanisms. *Inorg. Chem. Commun.* **2024**, *170*, 113496. [Google Scholar] [CrossRef]
25. Fu, R.; Liu, Y.; Lou, Z.; Wang, Z.; Baig, S.A.; Xu, X. Adsorptive removal of Pb(II) by magnetic activated carbon incorporated with amino groups from aqueous solutions. *J. Taiwan Inst. Chem. Eng.* **2016**, *62*, 247–258. [Google Scholar] [CrossRef]
26. Shikuku, V.O.; Mishra, T. Adsorption isotherm modeling for methylene blue removal onto magnetic kaolinite clay: A comparison of two-parameter isotherms. *Appl. Water Sci.* **2021**, *11*, 103. [Google Scholar] [CrossRef]
27. Lan, C.; Zhang, Y.; Li, Z.; Han, J.; Zhang, M.; Zhu, Y. Comparative investigation of two multivalent iron coexisting heterogeneous catalysts (Fe_3O_4/SC and ZVI/SC) activating H_2O_2 for enhanced MG dye wastewater purification: Performance and mechanism insights. *Colloids Surf.* **2026**, *746*, 140832. [Google Scholar] [CrossRef]
28. Xiang, H.; Ren, G.; Zhong, Y.; Xu, D.; Zhang, Z.; Wang, X.; Yang, X. Fe_3O_4@C nanoparticles synthesized by in situ solid-phase method for removal of methylene blue. *Nanomaterials* **2021**, *11*, 330. [Google Scholar] [CrossRef] [PubMed]
29. Zheng, Q.; Liu, X.; Tian, L.; Zhou, Y.; Liao, L.; Lv, G. Mechanism of Fenton catalytic degradation of Rhodamine B induced by microwave and Fe_3O_4. *Chin. Chem. Lett.* **2025**, *36*, 109771. [Google Scholar] [CrossRef]
30. Cao, C.; Guo, Y.; Chen, D.; Cui, J.; Hu, X. A MOF-derived $Fe_3O_4/Fe^0/Fe_3C$-2-600 dual-cathode electro-Fenton system construction: Revealing the mechanism for active centers linked by Fe^0 as an electronic transfer station for enhancing Fenton reaction. *Chem. Eng. J.* **2025**, *507*, 160710. [Google Scholar] [CrossRef]
31. Chen, Y.; Su, R.; Xu, F.; Ma, M.; Wang, Y.; Ma, D.; Li, Q. Oxygen-containing functional groups in Fe_3O_4@three-dimensional graphene nanocomposites for enhancing H_2O_2 production and orientation to $^1O_2$ in electro-Fenton. *J. Hazard. Mater.* **2024**, *470*, 134162. [Google Scholar] [CrossRef] [PubMed]
32. Wang, W.; Yan, J.; Ye, M.; Lin, H.; Dai, B.; Han, S. Response surface methodology optimization of Fe_3O_4@SiO_2-C_8 Pickering emulsion cutting fluids based on friction index and cooling index. *Colloids Surf.* **2026**, *748*, 141048. [Google Scholar] [CrossRef]
33. Sun, X.; Ni, X.; Wang, X.; Xu, D. Preparation of zero-valent iron-based composite catalyst with red mud and scrap tire as starting materials for Fenton-like degradation of methyl blue. *Surf. Interfaces* **2022**, *31*, 102053. [Google Scholar] [CrossRef]
34. Dangwang, J.M.D.; Oudou, N.; Dalhatou, S.; Mouhamadou, S.; Caperaa, C.; Kane, A.; Bonet, P.; Noumi, G.B.; Zhao, X. Enhanced photocatalytic degradation of naphtol blue black using CuO/g-C_3N_4 composite with persulphate: Optimization of the process by response surface methodology. *J. Water Process Eng.* **2026**, *83*, 109576. [Google Scholar] [CrossRef]
35. Kareem, R.; Afkhami, A.; Aziz, K.H.H. Synthesis of a novel magnetic biochar composite enhanced with polyaniline for high-performance adsorption of heavy metals: Focus on Hg(II) and Cu(II). *RSC Adv.* **2025**, *15*, 20309–20320. [Google Scholar] [CrossRef] [PubMed]
36. Yang, X.; Zhang, H.; Dai, X.; Zhang, H.; Zhang, Y.; Sun, D.; Tian, W. Degradation of rhodamine B using a heterogeneous Fenton-like reaction driven by nano-zero-valent iron loaded on biochar prepared in the presence of ultrasonic irradiation. *RSC Adv.* **2026**, *16*, 11655. [Google Scholar] [CrossRef] [PubMed]
37. Liu, L.; Yu, R.; Zhao, S.; Cao, X.; Zhang, X.; Bai, S. Heterogeneous Fenton system driven by iron-loaded sludge biochar for sulfamethoxazole-containing wastewater treatment. *J. Environ. Manag.* **2023**, *335*, 117576. [Google Scholar] [CrossRef] [PubMed]
38. Wang, Y.; Zhao, D.; Feng, S.; Chen, Y.; Xie, R. Ammonium thiocyanate functionalized graphene oxide-supported nanoscale zero-valent iron for adsorption and reduction of Cr(VI). *J. Colloid Interface Sci.* **2020**, *580*, 345–353. [Google Scholar] [CrossRef] [PubMed]
39. Ghazanchaie, S.; Kani, E.N.; Sangari, Z.A. Modeling the azo-dye removal from aqueous solution by adsorption on expanded modified vermiculite using statistical design and neural network. *Results Chem.* **2026**, *27*, 103410. [Google Scholar] [CrossRef]
40. Chen, M.; Guo, Q.; Pei, F.; Chen, L.; Rehman, S.; Liang, S.; Dang, Z.; Wu, P. The role of Fe(III) in enhancement of interaction between chitosan and vermiculite for synergistic co-removal of Cr(VI) and Cd(II). *Colloids Surf. A Physicochem. Eng. Asp.* **2020**, *606*, 125356. [Google Scholar] [CrossRef]
41. Bai, R.; Liu, S.; Han, J.; Wang, M.; Gao, W.; Wu, D.; Zhou, M. Expanded vermiculite supported capric-palmitic acid composites for thermal energy storage. *RSC Adv.* **2023**, *13*, 17516–17525. [Google Scholar] [CrossRef] [PubMed]
42. Luo, W.; Wang, C.; Zhang, Y.; Wu, L.; Qu, C. Silicate-modified nanoscale zero-valent iron supported on biochar activates peroxymonosulfate toward non-radical degradation of tetrabromobisphenol A. *Sep. Purif. Technol.* **2026**, *401*, 138540. [Google Scholar] [CrossRef]

43. Mahmuda, N.F.; Raharjo, Y.; Adiarto, T.; Darmokoesoemo, H.; Pramono, H.; Ismail, A.F. Green-synthesized zeolite Y-supported zero-valent iron nanocomposite for enhanced adsorptive reduction of hexavalent chromium from aqueous solutions. *RSC Adv.* **2026**, *16*, 26155–26164. [Google Scholar] [CrossRef] [PubMed]
44. Gao, R.; Hu, P.; Dai, Y.; Zhang, Y.; Liu, L.; Yang, W. Removal of cadmium(II) from aqueous solutions by a novel sulfide-modified nanoscale zero-valent iron supported on kaolinite: Treatment efficiency, kinetics and mechanisms. *Appl. Surf. Sci.* **2022**, *602*, 154353. [Google Scholar] [CrossRef]
45. Xiong, J.; Li, G.; Hu, C. Treatment of methylene blue by mesoporous Fe/SiO_2 prepared from rice husk pyrolytic residues. *Catal. Today* **2020**, *355*, 529–538. [Google Scholar] [CrossRef]
46. Sang, F.; Yin, Z.; Wang, W.; Almatrafi, E.; Wang, Y.; Zhao, B.; Gong, J.; Zhou, C.; Zhang, C.; Zeng, G.; et al. Degradation of ciprofloxacin using heterogeneous Fenton catalysts derived from natural pyrite and rice straw biochar. *J. Clean. Prod.* **2022**, *378*, 134459. [Google Scholar] [CrossRef]
47. Chen, S.; Ji, J.; Zhang, F.; Wang, B.; Liu, L.; Qin, J.; Hu, X. Chloride-enhanced degradation of diethyl phthalate in nano- and micro-scale zero valent iron-activated peroxydisulfate system: Transformation and regulation of Fe(IV) and free radicals. *J. Environ. Chem. Eng.* **2026**, *14*, 122902. [Google Scholar] [CrossRef]

Disclaimer/Publisher's Note: The statements, opinions and data contained in all publications are solely those of the individual author(s) and contributor(s) and not of MDPI and/or the editor(s). MDPI and/or the editor(s) disclaim responsibility for any injury to people or property resulting from any ideas, methods, instructions or products referred to in the content.